HHS Public Access

Author manuscript

Magn Reson Med. Author manuscript; available in PMC 2017 August 01.

Published in final edited form as:

Magn Reson Med. 2016 August ; 76(2): 613–625. doi:10.1002/mrm.25906.

Validation of a T_1 and T_2* leakage correction method based on multi-echo DSC-MRI using MION as a reference standard

Ashley M. Stokes, PhD[1,2], **Natenael Semmineh**[2,3], and **C. Chad Quarles, PhD**[1,2,*]

[1]Department of Radiology and Radiological Sciences, Vanderbilt University, Nashville Tennessee 37232, USA

[2]Institute of Imaging Science, Vanderbilt University, Nashville Tennessee 37232, USA

[3]Department of Physics, Vanderbilt University, Nashville Tennessee 37232, USA

Abstract

Purpose—A combined biophysical- and pharmacokinetic-based method is proposed to separate, quantify, and correct for both T_1 and T_2* leakage effects using dual-echo DSC acquisitions to provide more accurate hemodynamic measures, as validated by a reference intravascular contrast agent (CA).

Methods—Dual-echo DSC-MRI data were acquired in two rodent glioma models. The T_1 leakage effects were removed and also quantified in order to subsequently correct for the remaining T_2* leakage effects. Pharmacokinetic, biophysical, and combined biophysical and pharmacokinetic models were used to obtain corrected cerebral blood volume (CBV) and cerebral blood flow (CBF), and these were compared with CBV and CBF from an intravascular CA.

Results—T_1-corrected CBV was significantly overestimated compared to MION CBV, while T_1+T_2*-correction yielded CBV values closer to the reference values. The pharmacokinetic and simplified biophysical methods showed similar results and underestimated CBV in tumors exhibiting strong T_2* leakage effects. The combined method was effective for correcting T_1 and T_2* leakage effects across tumor types.

Conclusions—Correcting for both T_1 and T_2* leakage effects yielded more accurate measures of CBV. The combined correction method yields more reliable CBV measures than either correction method alone, but for certain brain tumor types (e.g., gliomas) the simplified biophysical method may provide a robust and computationally efficient alternative.

Keywords

contrast agent leakage; tumor hemodynamics; leakage correction; dynamic susceptibility-contrast MRI; perfusion imaging; biophysical model

*Corresponding author: C. Chad Quarles, Department of Radiology and Radiological Sciences and Institute of Imaging Science, Vanderbilt University, 1161 21st Ave. S., AA-1105 MCN, Nashville Tennessee 37232, USA, chad.quarles@vanderbilt.edu, (615) 322-6215.

Introduction

Dynamic susceptibility contrast (DSC) MRI in stroke and tumor has the potential to report on clinically useful diagnostic and therapeutic outcomes (1-7). In various pathologies, however, a compromised blood-brain barrier (BBB) leads to extravasation of gadolinium-based contrast agents (CA) and can severely alter the derived perfusion measures cerebral blood volume (CBV) and flow (CBF) and mean transit time (MTT) (7,8). Of the derived parameters, CBV is both the most reported and the most affected by CA extravasation (8), although CBF may also be affected to a smaller degree (9,10). There are three main sources of error that occur as a result of CA extravasation. First, as CA leaks out of the vasculature, it shortens the extravascular extracellular water T_1, leading to increased post-bolus signals and thus decreased post-bolus ΔR_2*. This results in underestimations of CBV. Second, leakage of CA also leads to T_2* effects due to changes in the susceptibility differences between the various compartments (e.g., intravascular to extravascular-extracellular or intracellular to extracellular) (11,12). As these effects depend on the CA compartmentalization, the resulting signals can be either increased or decreased but typically manifest as decreased signals (11,13). This leads to increased post-bolus ΔR_2* and thus overestimations of CBV. Finally, the central volume theorem underpinning DSC-MRI states that CBV is proportional to the flow-scaled integral of the capillary residue function, under the explicit assumption that the CA remains intravascular (14). In cases of CA extravasation, this is clearly violated, and uncorrected CBV values reflect the altered (larger) CA distribution volume (7,10).

Several methods have been proposed to reduce or remove leakage effects. The focus historically has been on T_1 leakage effects, where signal- and sequence-based methods (including pre-load bolus, low flip angle, gamma-variate fitting) have reduced T_1 sensitivity (8). Pharmacokinetic model-based correction methods have also been proposed (7,15,16). The most widely-used Weisskoff method estimates the leakage effects by comparing tumor ΔR_2* curves to those in a reference non-enhancing tissue, and the estimated leakage effects are then subtracted (2,7,16-18). Using this method, Boxerman et al. (7) showed that relative CBV (rCBV) correlates with glioma grade only when corrected for CA leakage. While this method is easy to implement, it assumes an identical MTT between the tumor and reference tissue, leading to potentially incorrect hemodynamic measures (19). An alternative approach later proposed by Bjornerud et al. (15) is based on a modified dynamic-contrast-enhanced (DCE) pharmacokinetic model that combines perfusion and permeability (20), resulting in a MTT-insensitive CBV correction method. This method is performed following deconvolution of the tissue residue function with the arterial input function (AIF), and existing challenges for this method include both accurate determination of the AIF and improved deconvolution stability in regions of low SNR. Moreover, CBF is not corrected for leakage effects as the model assumes the CA remains intravascular during the initial capillary transit phase (10,15). The corrections originally proposed by Weisskoff and Bjornerud are both potentially problematic because they simultaneously correct for both T_1 and T_2* leakage effects by relying on single echo data. Such data may exhibit competing T_1 and T_2* leakage effects whose biophysical bases are inherently dissimilar and require unique correction strategies that are not accounted for in pharmacokinetic models.

Dual- or multi-echo sequences (9,21,22) separate the T_1 leakage effects to provide both T_1-insensitive ΔR_2* time series and T_1-weighted signals extrapolated to TE=0. These dual-echo sequences are now recommended for DSC-MRI to obtain T_1-insensitive gradient-echo hemodynamic measures (8). As the dual-echo acquisition removes T_1 leakage effect, it also isolates (and enhances sensitivity to) the T_2* leakage effects, which can then be corrected by subsequent leakage correction methods. Previously, Schmiedeskamp et al. (10) utilized dual-echo-derived T_1-weighted signals to correct for T_2* leakage effects by combining the biophysical method proposed by Quarles (11) and the pharmacokinetic method proposed by Bjornerud (15). As with the original Bjornerud correction, this CBV correction method relies on sophisticated pharmacokinetic modeling and multistep fitting algorithms and does not correct CBF for leakage effects (10,15).

The primary focus of this study is to establish a MTT-insensitive leakage correction method for CBV and CBF that accounts for the biophysical basis of T_2* leakage effects. The biophysical model (11) underlying this method treats the observed ΔR_2* as a sum of the intra- and extravascular ΔR_2* components. Using a dual-echo acquisition to estimate the extravascular ΔR_2* component, the T_1-insensitive dual-echo ΔR_2* can be corrected for T_2* leakage effects. Corrections are performed using both a simplified biophysical model and a combined biophysical-pharmacokinetic model, and these corrections are compared to a purely pharmacokinetic model based on the Weisskoff method. Corrected CBF and CBV are shown in two rat brain tumor models exhibiting different combined T_1 and T_2* leakage effects. The resulting CBF and CBV are compared to reference standard CBF and CBV from injection of an intravascular iron oxide contrast agent in the same animals during the same imaging session.

Theory

As CA flows through blood vessels during bolus passage, it induces strong T_2* effects due to susceptibility gradients between the contrast-containing intravascular space and contrast-free extravascular space. However, in areas of BBB breakdown, leakage of CA out of the intravascular space and into the extravascular space leads to additional T_1 and T_2* relaxation effects. Due to the increased sensitivity to T_2* effects using dual-echo sequences, it is well known that CA leakage leads to increased ΔR_2* as a result of mesoscopic effects of CA compartmentalization around cells (12), resulting in overestimations of CBV. One approach to correct for these effects is to apply a pharmacokinetic model to the acquired ΔR_2* data to estimate the vascular and extravascular contributions simultaneously (10,13,23) and derive corrected estimates of CBV. As an alternative strategy, we propose an approach that provides leakage-corrected ΔR_2* time courses that may be subsequently analyzed using existing deconvolution analysis software or algorithms. Similar to previous studies (11,13,23), an empirical linear model is used to describe the measured ΔR_2* data as the sum of the vascular and extravascular contributions:

$$\Delta R^*_{2,\mathrm{meas}}(t) = r^*_{2,p} v_p C_p(t) + r^*_{2,e} v_e C_e(t) \quad [1]$$

where $r^*_{2,p}$ and $r^*_{2,e}$ are the T_2* relaxivities for plasma and extravascular-extracellular space (EES), respectively, and v_p, C_p, v_e, and C_e are the volume fractions and CA concentrations of the EES and blood plasma, respectively. (A full list of relevant parameters can be found in Table S1 in the Supporting Material.) The first term represents the intravascular ΔR_2* contribution while the second term represents the extravascular ΔR_2* contribution that presents as a result of CA leakage. The T_2* relaxivities are related to the geometric features of the vascular ($r^*_{2,p}$) and extravascular extracellular ($r^*_{2,e}$) compartments. Of particular interest, $r^*_{2,e}$ predominantly reflects the underlying cellular features that define the spatial boundaries or geometry of the CA distribution volume. This is in contrast to T_1 leakage effects, which reflect the direct interaction of the CA with water in the EES and can be characterized by the CA's T_1 relaxivity and traditional pharmacokinetic models. Because cellular features (e.g., density, spacing, size, shape) vary within and across tumors, a simple pharmacokinetic treatment of T_2* leakage effects may be unable to accurately characterize and remove their confounding influence on DSC-MRI data. This implies that efforts to correct T_2* leakage effects should include voxel-wise estimates of $r^*_{2,e}$.

To isolate the intravascular ΔR_2* term, the extravascular ΔR_2* contribution ($r^*_{2,e} v_e C_e(t)$) can be calculated and then subtracted from the measured ΔR_2*. This requires estimation of both $r^*_{2,e}$ and $v_e C_e(t)$ as follows. From dual-echo DSC-MRI, a T_1-weighted signal can be combined with a pre-contrast T_1 map to obtain the tissue CA concentration ($C_t = \Delta R_1 / r_1$), where r_1 is the CA T_1 relaxivity. The extended Tofts model (24,25) can be applied to isolate the contribution of $v_e C_e(t)$ to the total tissue CA concentration ($C_t(t)$). As Sourbron et al. (23) has previously shown, the effective extravascular T_2* relaxivity $r^*_{2,e}$ can be obtained by fitting the dual-echo ΔR_2* to the appropriate model (given here by Eq. 1), where $v_e C_e(t)$ and $v_p C_p(t)$ are inputs from the extended Tofts model and the only unknowns are $r^*_{2,e}$ and $r^*_{2,p}$. The corrected ΔR_2* can be thus computed using

$$\Delta R^*_{2,\mathrm{corr}}(t) = \Delta R^*_{2,\mathrm{meas}}(t) - r^*_{2,e} v_e C_e(t) \quad [2]$$

The equations shown in [1] and [2] are similar in form to the Weisskoff leakage correction strategy (2,7,16-18), where the corrected ΔR_2* is computed as the difference between the measured time series and an estimate of the dynamic leakage effects. These leakage effects are estimated using a scaled version of the time integral of ΔR_2*(t) taken from non-enhancing tissue, which implies that the extravascular contrast agent concentration time courses across tumor voxels are scaled versions of the same underlying profile. By leveraging the ΔR_1 information provided by dual-echo DSC-MRI signals, a similar heuristic leakage correction approach can be derived that quantifies the voxel-wise contrast agent concentration profiles, thereby accounting for local heterogeneity in the underlying contrast agent kinetics.

For this simplified approach, the extravascular ΔR_2* contribution is approximated as $r^*_{2,t} C_t(t)$. In this case, C_t is taken directly from $\Delta R_1 / r_1$ under the assumption that $C_t(t)$

predominantly reflects the extravascular CA concentration, similar to the conventional Tofts model (25,26) used for DCE-MRI that assumes negligible intravascular contribution. The dynamic $C_t(t)$ is scaled by $r^*_{2,t}$, which is the effective tissue transverse CA relaxivity. As previously shown, when computed at CA equilibrium, $r^*_{2,t}$ is insensitive to the vasculature because there is no susceptibility difference between the intra- and extravascular space (12); thus as for $r^*_{2,e}$, $r^*_{2,t}$ predominantly reflects cellular features. The $r^*_{2,t}$ can be calculated voxel-wise from simultaneously acquired dual-echo ΔR_2^* and ΔR_1 data. Using the ΔR_1 information to calculate the tissue CA concentration ($C_t = \Delta R_1/r_1$), $r^*_{2,t}$ can be computed as:

$$r^*_{2,t} = \frac{\Delta R^*_{2,\mathrm{meas}}}{C_t} = \frac{r_1 \cdot \Delta R^*_{2,\mathrm{meas}}}{\Delta R_1} \quad [3]$$

Similar in form to the correction provided by Eq. [2] and the Weisskoff approach, the corrected ΔR_2^* can be computed using:

$$\Delta R^*_{2,\mathrm{corr}}(t) = \Delta R^*_{2,\mathrm{meas}}(t) - r^*_{2,t} C_t(t) \quad [4]$$

Note that the proposed correction strategies described in Eqs. [2] and [4] do not rely upon estimates of a given voxel's CA concentration time course or the effective contrast agent relaxivity, such as that used in the Weisskoff correction of single-echo DSC-MRI data (7,16,18). Rather, these methods leverage the dual-echo based ΔR_2^* and ΔR_1 data in order to measure these parameters.

Methods

Simulations

To demonstrate the validity of the proposed simplified T_2^* leakage correction technique, a computational study was conducted based on simulated 3D tissue structures composed of randomly packed ellipsoids around fractal tree based vascular networks using the finite perturber finite difference method (FPFDM) (27). First, a pharmacokinetic two-compartmental model described in (28) was used to compute the vascular and EES CA concentration (C_p and C_e) time-courses using physiologically relevant CBV, CBF, K^{trans} and v_e values along with the AIF as an input. The resulting C_p and C_e curves, the simulated tissue structures, the water diffusion coefficient, and relevant pulse sequence parameters were then used to compute simulated ΔR_2^* time curves using the FPFDM. The effective tissue relaxivity $r^*_{2,t}$ was calculated using time points at CA concentration equilibrium, allowing computation of the corrected ΔR_2^* time-courses according to Eqs. [2] and [4].

Animals Methods

All animal studies were performed in accordance with National Institutes of Health (NIH) Institutional Animal Care and Use Committee (IACUC) protocols. For all procedures and

imaging, the animals were immobilized in a stereotactic head holder. Anesthesia was induced using 3-5% isoflurane in air and maintained with 1-2.5% isoflurane in air. Body temperature was maintained at 38°C using forced warm air. Male Fischer (n=12) and Wistar (n=9) rats (Harlan Laboratories, Indianapolis, IN) were inoculated with 1×10^5 9L and C6 glioma cells (American Type Culture Collection, Manassas VA), respectively, at 1 mm anterior and 3 mm lateral to the bregma and 4 mm depth from the dural surface. Imaging was performed after 16 days.

MRI Methods

MRI was performed at 4.7T (Agilent, Santa Clara, CA). Pre-contrast T_1 maps were acquired using an inversion recovery (IR) snapshot FLASH GE sequence (8 inversion times exponentially spaced from 250 ms to 6 s, TR = 8 s, TE = 2.9 ms, and $\alpha = 15°$). A spin- and gradient-echo (SAGE) EPI sequence was used to obtain five echoes (10,29,30), including two gradient echoes (dual-echo). Standard slice-selective sinc pulses were used. A 64×64 acquisition matrix within a 36×36 mm^2 FOV was acquired with 8 1-mm thick slices. Partial Fourier encoding (48 of 64 lines acquired) was used to obtain acceptable gradient echo times (TE_1 and TE_2 = 8.6 and 35 ms). The partially sampled k-space data were reconstructed to full Fourier space using an iterative homodyne reconstruction algorithm (31,32) in Matlab (Mathworks, Inc.). To obtain adequate temporal resolution for dynamic studies, a TR of 1 s was used for 10 minutes. After 80 s of baseline images, 0.4 mmol/kg gadolinium-diethylenetriamine pentaacetic acid (Gd-DTPA) was injected via jugular catheter. After 30 minutes to allow partial Gd-DTPA clearance, 3 mg/kg MION was injected via a second jugular catheter. The MION was diluted with sterile saline to provide an equal injection volume to the Gd-DTPA injection.

Post-processing and Analysis

To increase the SNR, the DSC data was first reconstructed to 2-mm slice thickness by averaging the signal of two consecutive slices. The first two (gradient) echoes were used to calculate the T_1-insensitive dual-echo ΔR_2*. All leakage correction methods were applied to dual-echo data, which is inherently corrected for T_1 leakage. Thus, the ability of the corrections methods to correct for T_2* leakage effects was determined. Three methods of leakage correction were compared: a pharmacokinetic model based on the Weisskoff method (Method 1) and two variations of the biophysical model proposed herein (Methods 2 and 3). Method 2 utilizes the simplified biophysical model in Eq. 4, while Method 3 combines biophysical and pharmacokinetic methods (Eq. 2).

In Method 1, the corrected ΔR_2* curve is obtained by fitting the measured ΔR_2* curve to a reference, whole brain non-enhancing curve to determine the leakage-relevant parameter. As in the original implementations for single echo data, the whole brain non-enhancing mask was created by comparing the signal from TE_2 during the post-bolus phase (90 s post-injection) to the pre-bolus signal. Voxels with post-bolus signal that was greater than or less than one standard deviation from the prebolus mean signal were excluded from the whole-brain non-enhancing mask. The mask was applied to the dual-echo data to create the reference curve $\overline{\Delta R_2^*(t)}$ and its time integral $\int_0^t \overline{\Delta R_2^*(t')} dt'$. The measured dual-echo ΔR_2* was fit to Equation 5 to obtain the leakage parameter K_2:

$$\Delta R_2^*(t) \approx K_1 \cdot \overline{\Delta R_2^*(t)} - K_2 \int_0^t \overline{\Delta R_2^*(t')} dt' \quad [5]$$

Consistent with correction of both T_1 and T_2* leakage effects (7,17), K_2 was permitted to have positive or negative values. In contrast to prior implementations, Method 1 did not utilize a pre-load bolus to reduce T_1 leakage effects, as this would preclude analysis using Method 2, but rather the correction was applied to T_1-insensitive dual-echo data.

In Method 2, the corrected ΔR_2* curve was obtained by subtracting a voxel-wise estimate of $r_{2,t}^* C_t(t)$ (Eq. [4]). To approximate C_t, the dual-echo T_1–weighted signals were combined with a pre-contrast T_1 map to obtain a ΔR_1 curve, as previously described (30,33). To convert ΔR_1 to C_t, a r_1 relaxivity of 3.9 $mM^{-1}s^{-1}$ for Gd-DTPA was used (34). The effective tissue transverse relaxivity ($r_{2,t}^*$) in the EES at CA equilibrium was determined from the mean voxel-wise dual-echo ΔR_2* and ΔR_1 at 1 minute intervals from 2 to 8 minutes post-injection to determine the optimal range of scan times for calculation of $r_{2,t}^*$ (Supporting Material, Figure S1). Subsequently, $r_{2,t}^*$ was calculated from 5 to 6 minutes post-injection. The voxel-wise extravasation term $r_{2,t}^* C_t(t)$ was subtracted from the corresponding dual-echo ΔR_2* to determine the T_1- and T_2*-leakage corrected ΔR_2*.

In Method 3, the corrected ΔR_2* curve was obtained by subtracting a voxel-wise estimate of $r_{2,e}^* v_e C_e(t)$ (Eq. [2]). The tissue CA concentration $C_t(t)$ was estimated as in Method 2. Using the extended Tofts model (24), $v_e C_e(t)$ was obtained by fitting $C_t(t)$:

$$C_t(t) = v_p C_p(t) + v_e C_e(t) = v_p C_p(t) + K^{\text{trans}} \int_0^t C_p(\tau) \cdot e^{-K^{\text{trans}} \cdot (t-\tau)/v_e} d\tau \quad [6]$$

The vascular input function $C_p(t)$ was determined from the ΔR_1 data (35) and was scaled until $C_t(t)$ in muscle yielded a v_e of 0.11 (36). Voxels with non-physiological volume fractions ($v_{p,e} < 0$ or $v_{p,e} > 1$) were set to zero and were not used for subsequent analysis. The extravascular CA T_2* relaxivity $r_{2,e}^*$ was obtained by fitting the dual-echo ΔR_2* to Equation 1, where $v_e C_e$ and $v_p C_p$ are inputs from the extended Tofts model and the only unknowns are $r_{2,e}^*$ and $r_{2,p}^*$. The voxel-wise extravasation term $r_{2,e}^* v_e C_e(t)$ was subtracted from the corresponding dual-echo ΔR_2* to determine the T_1- and T_2*-leakage corrected ΔR_2*.

The dual-echo (T_1-corrected) ΔR_2* was used for determination of the arterial input function (AIF), which was selected using an automated method (37) specifically adapted for use with multi-echo acquisitions (38). An adaptive threshold based on image SNR (39) was used for deconvolution. CBF was taken as the maximum of the impulse response function determined from the circular singular value decomposition (SVD) of the AIF and tissue ΔR_2* (40). CBV was determined from the ratio of the scaled integrals of the tissue ΔR_2* curve and the arterial input function curve. For display purposes in Figure 3, CBV and CBF were

normalized to 4% and 60 ml/100g/min in gray matter. For subsequent figures, CBV and CBF are given relative to contralateral normal tissue, as indicated using rCBV and rCBF.

The Gd-DTPA DSC measures were obtained using 120 points (= 120s) of data, with 60s before and 60s after injection. To match the number of points included following bolus passage to the Gd-DTPA analysis, the MION DSC measures were obtained using 110 points (= 110s) of data, with 60s before and 50s after injection. The T_1-corrected (dual-echo) and T_1- and T_2*-corrected (Method 1 based on the Weisskoff correction and Methods 2 and 3 proposed herein) Gd-DTPA-based DSC parameters were compared to the MION-based DSC parameters. To match the Gd-DTPA analysis, the MION DSC parameters were obtained from the dual-echo signals.

Mean transit time sensitivity

To determine how sensitive Method 1 is to MTT variations, percent error in rCBV was determined as a function of MTT. To this end, MTT bins were created for low, mid, and high MTT using the mean and standard deviation (std) of the normal tissue MTT. More specifically, voxels with MTT less than 1 std from the normal tissue MTT were binned into the low MTT bin; voxels with MTT within 1 std of the normal tissue MTT were binned into the mid MTT bin; voxels with MTT greater than 1 std higher than the normal tissue MTT were binned into the high MTT bin. These bins were then used to determine the rCBV percent error for dual-echo and Methods 1, 2, and 3.

Statistical Analysis

Data analysis was performed on regions of interest (ROIs) that were initially drawn from T_2-weighted fast spin echo (FSE) images at a long TE (80ms), with the tumor ROIs further refined using a 15% enhancement threshold compared to the normal tissue ROIs. Voxels with non-physiological volume fractions were excluded from the ROI analysis. The perfusion parameters are reported as group mean ± std for the 9L and C6 tumor types. Concordance correlation coefficient (CCC) and Pearson's correlation coefficient (R) were used to assess linear agreement, with the former used as a measure of accuracy and the latter as a measure of precision. Significance was tested using a paired t-test between the MION DSC parameters and the dual-echo (T_1-corrected only) and T_1- and T_2*-corrected DSC parameters. Results were considered significant at $p<0.05$.

Results

Figure 1 demonstrates the simulated time-courses (a-c) for a given vascular volume fraction of 8% and cell volume fraction of 60%. The CA concentration in the plasma and EES are shown in Figure 1a, along with the corresponding ΔR_2* time-courses for no leakage, uncorrected, C_t corrected, and $v_e C_e$ corrected simulations (Figures 1b-c). CA leakage leads to elevated ΔR_2*, while correction with C_t overcorrects the leakage effects and leads to underestimated ΔR_2*. Note that the inclusion of the $v_p C_p$ term in C_t causes a large underestimation in the peak amplitude. Correction with $v_e C_e$ yields ΔR_2* time-courses that most closely resembles the ΔR_2* observed for the CA contained within the vessels, with only slight effects on the peak amplitude. Figure 1d compares the CBV percent difference

between no leakage and the uncorrected CBV, C_t corrected CBV, and $v_e C_e$ corrected CBV. The uncorrected CBV strongly overestimates the true CBV for all v_p values, while both corrections come closer to the true CBV. Corrections using C_t tend to underestimate CBV, with increasing error for increasing vascular volume contributions. Corrections using $v_e C_e$ yield CBV measurements that are within 15% of the true CBV for all v_p values.

Figure 2 shows example time-courses in a 9L tumor (top) and C6 tumor (bottom) using Gd-DTPA (left) and MION (right) CA. The AIF in each case is also shown, which tends to be higher and narrower, peaking earlier, than the time-courses in normal and tumor tissue. The dual-echo ΔR_2* in the 9L tumor showed clear T_2* leakage effects, manifesting as extremely elevated post-bolus ΔR_2*. On the other hand, the dual-echo ΔR_2* in the C6 tumor exhibited minimal T_2* leakage effects. The Gd-DTPA exhibited a wider FWHM than MION despite having identical injection volumes and speeds, which can be attributed to the higher viscosity of the Gd-DTPA. The DSC analysis limits of 60 s post-bolus for Gd-DTPA and 50 s post-bolus for MION are also shown, where these limits were chosen to match the number of points included following bolus passage.

Figure 3 compares the effects of each leakage correction method on 9L (top) and C6 (bottom) tumor time-courses. The 9L tumor showed strong T_2* leakage effects in the dual-echo ΔR_2*, and these were corrected differently with each method (Methods 1-3, left to right). The shapes of the leakage terms in each method are dissimilar, leading to different corrected ΔR_2* time-courses. In particular, the corrections given by Methods 1 and 2 reduce the ΔR_2* more substantially than that provided by Method 3 during the initial bolus passage. Although the dual-echo ΔR_2* in the C6 tumors appeared relatively normal, all correction methods changed the ΔR_2* time courses indicating the presence of T_2* leakage effects. Note that because Methods 1 and 3 involve data fitting to obtain the leakage term, this term is artificially smoother than the voxel-based leakage term in Method 2. Fitting the C_t curve to the standard Tofts model would yield smoothed curves similar to Methods 1 and 3.

The CBV and CBF maps in 9L (top rows) and C6 (bottom rows) tumors are shown in Figure 4 for T_1-corrected dual-echo, Methods 1, 2, and 3, and MION. The dual-echo CBV was overestimated compared to the MION CBV for the 9L due to strong T_2* leakage effects, while the dual-echo CBV was fairly close to the MION CBV in the T_1-dominant C6 tumors. In the 9L tumors, the T_1- and T_2*-corrected CBV maps using Methods 1-3 much more closely matched that of MION. All three methods performed comparably in the C6 tumor. CBF was fairly consistent across dual-echo and methods 1 and 2, indicating only minor effects of leakage of CBF. In general, CBF was slightly underestimated using Gd-DTPA compared to MION.

Figure 5 shows plots of rCBV from T_1-corrected dual-echo and Methods 1-3 versus MION rCBV in both tumor types. Dual-echo rCBV is highly overestimated for both 9L and C6 tumors, while the corrected rCBVs with Methods 1-3 generally provided linear fits closer to the line of unity. Table 1 summarizes the Gd-DTPA and MION mean (std) rCBV and rCBF for all 9L and C6 tumors. The parameters (slope, CCC, R, and p-value) from the linear fits of each correction method versus MION are also summarized in Table 1. Leakage correction

substantially improved the Gd-DTPA rCBV compared to MION. Leakage correction did not significantly change rCBF, which was underestimated for all measures relative to MION.

The bar plots in Figure 6 show rCBV and rCBV percent error in 9L and C6 tumors using dual-echo, Methods 1, 2, and 3, and reference MION measurements. With MION, the 9L and C6 tumors were both characterized by elevated rCBV and rCBF (Table 1). The 9L tumors typically had higher rMTT, while the C6 tumors were characterized by rMTTs similar to normal tissue. The Gd-DTPA rCBV in 9L tumors was significantly different from MION using dual-echo ($p < 0.01$), while Methods 1 and 2 significantly underestimated rCBV ($p < 0.01$). Method 3 provided a more reliable estimate of rCBV in 9L tumors and was not significantly different from MION ($p = 0.22$). Methods 1 and 2 were not significantly different, while both were significantly different from Method 3 ($p < 0.01$). In C6 tumors, the dual-echo rCBV was significantly overestimated ($p < 0.01$), while Methods 1-3 provided more reliable estimates of rCBV compared to MION ($p = 0.99$, 0.13, and 0.48, respectively). None of the correction methods (Method 1, 2, and 3) were significantly different from each other.

Bland-Altman plots (Figure 7) revealed a positive bias for dual-echo rCBV for both tumor types, and a general trend appeared as rCBV increased for dual-echo to overestimate the MION CBV. In 9L tumors, Methods 1 and 2 had a slight negative bias for rCBV, while Method 3 showed little to no bias. Methods 1-3 showed little to no bias for the C6 tumors.

Figure 8 shows the rCBV percent error as a function of MION MTT for MTT bins with low, mid, and high MTT relative to normal tissue MTT. In the 9L tumors, the low MTT bin comprised 3% of the tumor voxels, while the mid and high MTT bins comprised 68% and 29% of the tumor voxels, respectively. The dual-echo rCBV was significantly overestimated for all MTT bins ($p < 0.01$). All corrections methods (1-3) significantly overestimated rCBV for the low MTT bin. Methods 1 and 2 significantly underestimated rCBV for the mid and high MTT bins ($p < 0.05$), while Method 3 rCBV was not significantly different from MION rCBV ($p > 0.05$). For the C6 tumors, the low and mid MTT bins comprised 10% and 78% of the tumor voxels, respectively, while the high MTT bins comprised 12% of tumor voxels. Once again, dual-echo rCBV was overestimated for all MTT bins. In this tumor model, Methods 1 and 3 were not significantly different from MION rCBV for any MTT, while Method 2 was significantly different from MION in the high MTT bin.

Discussion

Previous reports have shown that single-echo DSC-MRI data, uncorrected for leakage effects, have complex combinations of T_1 and T_2* leakage effects (8,41) that can lead to unreliable measures of CBV and CBF. In this study, we have proposed a combined biophysical and pharmacokinetic approach for correcting both T_1 and T_2* leakage effects using multi-echo DSC data, as well as a further simplification of the proposed model that does not require pharmacokinetic modeling. Using this combined method, we have shown that T_1 and T_2* correction provides reliable perfusion parameters that are comparable to MION, while further simplifying this model may provide reasonable rCBV values without data fitting. In addition to comparisons with MION DSC-MRI, the methods proposed herein

(Methods 2 and 3) were compared to the pharmacokinetic correction method established by Weisskoff (Method 1). The Weisskoff method for correcting single-echo rCBV data with a pre-load was previously validated using steady-state MION CBV as the reference standard in 9L tumors (16).

In the present study, dynamic MION data permitted measurement of both CBF and CBV using similar perfusion analysis methods for both types of CA. Further, the correction reliability of each method was compared in two tumor models that exhibit dissimilar leakage effects. The 9L gliosarcoma tumors have substantial T_1 and T_2* leakage effects, while the C6 glioblastoma tumors have T_1-dominant leakage effects. In the 9L tumors, Method 3 provided the most reliable rCBV results, whereas Methods 1-3 provided similar rCBV values in the C6 tumors. The 9L tumors were also characterized by a high tumor MTT. MTT sensitivity is a known drawback of the Weisskoff method (19), and MTT heterogeneity has been previously noted in human tumors (10,15). Method 3 did not exhibit MTT dependence and may be applicable to a wider range of hemodynamic conditions. Despite its sensitivity to MTT, Method 1 provided similar perfusion parameters to Method 2, which tended to underestimate MION rCBV in the 9L tumors and agreed with MION rCBV in the C6 tumors. Gd-DTPA CBF was underestimated compared to MION CBF, and this was not altered by leakage correction, consistent with previous reports showing minor (9) or negligible (10,15) effects of CA leakage on CBF.

In contrast to prior implementations, Method 1 did not include a pre-load bolus to reduce T_1 leakage effects (7,16), as all three Methods were applied to T_1-insensitive dual-echo data to correct isolated T_2* leakage effects. As noted above, T_1 leakage effects can be effectively described by traditional pharmacokinetic models, as they derive from the direct interaction of tissue water with the CA, which has a known (or assumed) relaxivity. In contrast, T_2* effects are more complex, originating from increased magnetic field heterogeneity due to the compartmentalization of CA around cells (12,27). In the limiting cases of data only sensitive to either T_1 or T_2* leakage effects, this implies that the parameters K_2 and K_a from the Weisskoff and Bjornerud methods reflect, in the case of T_1 leakage effects, the degree of CA extravasation (e.g., a mixed measure of permeability and the volume fraction of the EES) or, in the case of T_2* leakage effects, a tissue's cellular properties (e.g., cell density, size, orientation, shape) and the local CA concentration. In practice, all single-echo based DSC-MRI data is a complex combination of competing T_1 and T_2* leakage effects and their presence depends on CA pharmacokinetics, tissue microstructure, and pulse sequence parameters. These potential confounds motivated the development of the leakage correction technique proposed herein, which has the advantages of eliminating T_1 leakage effects, quantifying voxel-wise CA concentration time curves, and using this information to estimate and remove T_2* leakage effects that depend upon the underlying tissue cytoarchitecture.

Several assumptions were made in our correction methods. The first assumption is that the empirical biophysical model (Equation 1) accurately describes the underlying biophysical basis of CA-induced T_2* leakage effects. This model itself is a simplification of the models proposed in Refs (10,13,23), where we assume that the gradient term is negligible relative to v_pC_p and v_eC_e, similar to Ref (10). In contrast, Soubron et al. (13,23) includes the gradient correction term in their biophysical model, which may be more accurate in describing the

underlying relaxivity contributions. The strong agreement between Method 3 and the MION CBV data indicate, at least in the context of these animal tumor models, that the gradient term has negligible influence on the measured leakage effects. In Method 2, we further assume that the measured ΔR_1 ($= r_1 \cdot C_t$) primarily reflects the CA in the EES. This assumption is tested in Method 3, where the tissue CA concentration is taken as a weighted sum of the plasma and EES concentrations ($C_t = v_p C_p + v_e C_e$), assuming again that the intracellular concentration is zero. The 9L tumors tend to be more vascular than the C6 tumors, which could explain why Method 2 tends to underestimate rCBV in the 9L tumors, while providing reasonable rCBV values in the C6 tumors. Another major assumption in Method 2 is that $r^*_{2,t}$ is a reasonable approximation for $r^*_{2,e}$. As previously shown (12), $r^*_{2,t}$ is highly sensitive to cellular properties, such as cell size and density. Although $r^*_{2,t}$ was found to be approximately 25-30% higher than $r^*_{2,e}$, this may be an acceptable assumption given the agreement with MION data. A final assumption is that the equilibrium relaxivity $r^*_{2,t}$ remains constant over the dynamic time course. This is unlikely to be a significant source of error as choosing different equilibrium points did not significantly alter our resulting CBF and CBV measures.

A potential limitation of our method is that reliable extraction of DCE-MRI based pharmacokinetic parameters requires acquisition times that are greater than traditional DSC-MRI scans (at least 5 minutes of post-contrast data) (42,43). However, the additional scan time has the advantage of enabling the simultaneous assessment of DSC- and DCE-MRI data (22). It should also be noted that the proposed technique assumes unidirectional CA transport out of the vasculature and may not be valid in highly permeable tissues, where CA from the EES re-enters the intravascular space. A final limitation of this study is that, as is typical in most DSC-MRI studies, literature values of arterial and vascular CA relaxivity were not used to convert ΔR_2* to CA concentration. As a result, quantitative absolute values for CBV and CBF could not be obtained.

Unlike these relative homogeneous animal models, human tumors exhibit a range of T_1 and T_2* leakage effects. From single-echo DSC-MRI studies (using moderate to high flip angles (60-90°) and typical echo times (> 40 ms), primary central nervous system lymphomas (PCNSL) predominantly exhibit T_1 leakage effects, gliomas mostly exhibit T_1 effects (approx. 60-70% of voxels), and brain metastasis primarily show T_2* effects (15,44). Accordingly, the results herein would suggest that for dual-echo DSC-MRI data acquired in PCNSL and gliomas, Methods 1-3 would yield similar rCBV results, but in brain metastases, Method 3 would provide the most reliable rCBV data. These observations, however, need to be validated in clinical studies.

Conclusions

In conclusion, we have demonstrated that dual-echo based CBV maps that are not corrected for T_2* leakage effects are unreliable. Correcting dual-echo DSC-MRI data using the only pharmacokinetic or biophysical models (Methods 1 and 2, respectively) yields underestimated rCBV in tumors with strong T_2* leakage effects and more reliable perfusion parameters in tumors with moderate T_2* leakage effects. By leveraging the dual-echo data to

compute the voxel-wise CA concentration time series and taking into account the biophysical basis of T_2* leakage effects, the combined pharmacokinetic and biophysical approach yields more reliable perfusion parameters. The simplified biophysical method (Method 2) is computationally efficient, as it requires no model fitting, which could ease its clinical translation for the assessment of brain tumor hemodynamic characterization and treatment response, particularly in the context of gliomas that show limited to moderate T_2* leakage effects.

Supplementary Material

Refer to Web version on PubMed Central for supplementary material.

Acknowledgments

We would like to thank Jack Skinner, PhD, and Jerry Boxerman, MD PhD, for many helpful discussions and Zou Yue for help with animal prep. This work was performed at the Vanderbilt University Institute of Imaging Science, with support from NCI P30 CA68485 and 1R01CA158079.

References

1. Boxerman JL, Hamberg LM, Rosen BR, Weisskoff RM. MR contrast due to intravascular magnetic susceptibility perturbations. Magn Reson Med. 1995; 34(4):555–566. [PubMed: 8524024]
2. Donahue KM, Krouwer HGJ, Rand SD, Pathak AP, Marszalkowski CS, Censky SC, Prost RW. Utility of simultaneously acquired gradient-echo and spin-echo cerebral blood volume and morphology maps in brain tumor patients. Magn Reson Med. 2000; 43(6):845–853. [PubMed: 10861879]
3. Aronen HJ, Gazit IE, Louis DN, Buchbinder BR, Pardo FS, Weisskoff RM, Harsh GR, Cosgrove GR, Halpern EF, Hochberg FH. Cerebral blood volume maps of gliomas: comparison with tumor grade and histologic findings. Radiology. 1994; 191(1):41–51. [PubMed: 8134596]
4. Sorensen AG, Emblem KE, Polaskova P, Jennings D, Kim H, Ancukiewicz M, Wang M, Wen PY, Ivy P, Batchelor TT, Jain RK. Increased Survival of Glioblastoma Patients Who Respond to Antiangiogenic Therapy with Elevated Blood Perfusion. Cancer research. 2012; 72(2):402–407. [PubMed: 22127927]
5. Sugahara T, Korogi Y, Kochi M, Ikushima I, Hirai T, Okuda T, Shigematsu Y, Liang L, Ge Y, Ushio Y, Takahashi M. Correlation of MR imaging-determined cerebral blood volume maps with histologic and angiographic determination of vascularity of gliomas. American Journal of Roentgenology. 1998; 171(6):1479–1486. [PubMed: 9843274]
6. Law M, Yang S, Babb JS, Knopp EA, Golfinos JG, Zagzag D, Johnson G. Comparison of Cerebral Blood Volume and Vascular Permeability from Dynamic Susceptibility Contrast-Enhanced Perfusion MR Imaging with Glioma Grade. AJNR American journal of neuroradiology. 2004; 25:746–755. [PubMed: 15140713]
7. Boxerman JL, Schmainda KM, Weisskoff RM. Relative Cerebral Blood Volume Maps Corrected for Contrast Agent Extravasation Significantly Correlate with Glioma Tumor Grade, Whereas Uncorrected Maps Do Not. Am J Neuroradiol. 2006; 27(4):859–867. [PubMed: 16611779]
8. Paulson ES, Schmainda KM. Comparison of Dynamic Susceptibility-weighted Contrast-enhanced MR Methods: Recommendations for Measuring Relative Cerebral Blood Volume in Brain Tumors. Radiology. 2008; 249(2):601–613. [PubMed: 18780827]
9. Vonken, EjPA.; van Osch, MJP.; Bakker, CJG.; Viergever, MA. Simultaneous quantitative cerebral perfusion and Gd-DTPA extravasation measurement with dual-echo dynamic susceptibility contrast MRI. Magn Reson Med. 2000; 43(6):820–827. [PubMed: 10861876]
10. Schmiedeskamp H, Andre JB, Straka M, Christen T, Nagpal S, Recht L, Thomas RP, Zaharchuk G, Bammer R. Simultaneous perfusion and permeability measurements using combined spin- and

gradient-echo MRI. Journal of cerebral blood flow and metabolism : official journal of the International Society of Cerebral Blood Flow and Metabolism. 2013; 33(5):732–743.

11. Quarles CC, Gochberg DF, Gore JC, Yankeelov TE. A theoretical framework to model DSC-MRI data acquired in the presence of contrast agent extravasation. Physics in medicine and biology. 2009; 54(19):5749–5766. [PubMed: 19729712]
12. Semmineh NB, Xu J, Skinner JT, Xie J, Li H, Ayers G, Quarles CC. Assessing tumor cytoarchitecture using multiecho DSC-MRI derived measures of the transverse relaxivity at tracer equilibrium (TRATE). Magn Reson Med. 2014; doi: 10.1002/mrm.25435
13. Sourbron S, Heilmann M, Biffar A, Walczak C, Vautier J, Volk A, Peller M. Bolus-tracking MRI with a simultaneous T1- and T2*-measurement. Magn Reson Med. 2009; 62(3):672–681. [PubMed: 19585599]
14. Barker, PB.; Golay, X.; Zaharchuk, G. Clinical Perfusion MRI: Techniques and Applications. Cambridge University Press; 2013.
15. Bjornerud A, Sorensen AG, Mouridsen K, Emblem KE. T1- and T2*-dominant extravasation correction in DSC-MRI: part I--theoretical considerations and implications for assessment of tumor hemodynamic properties. Journal of cerebral blood flow and metabolism: official journal of the International Society of Cerebral Blood Flow and Metabolism. 2011; 31(10):2041–2053.
16. Boxerman JL, Prah DE, Paulson ES, Machan JT, Bedekar D, Schmainda KM. The Role of preload and leakage correction in gadolinium-based cerebral blood volume estimation determined by comparison with MION as a criterion standard. AJNR American journal of neuroradiology. 2012; 33(6):1081–1087. [PubMed: 22322605]
17. Liu HL, Wu YY, Yang WS, Chen CF, Lim KE, Hsu YY. Is Weisskoff model valid for the correction of contrast agent extravasation with combined T_1 and T_2* effects in dynamic susceptibility contrast MRI? Medical Physics. 2011; 38(2):802. [PubMed: 21452717]
18. Weisskoff, RM.; Boxerman, JL.; Sorensen, AG.; Kulke, SM.; Campbell, TA.; Rosen, BR. Simultaneous blood volume and permeability mapping using a single Gd-based contrast injection. Proceedings of the 2nd Annual Meeting of SMRM; San Francisco, CA, USA. 1994; p. 279
19. Quarles CC, Ward BD, Schmainda KM. Improving the reliability of obtaining tumor hemodynamic parameters in the presence of contrast agent extravasation. Magn Reson Med. 2005; 53(6):1307–1316. [PubMed: 15906288]
20. St Lawrence KS, Lee TY. An Adiabatic Approximation to the Tissue Homogeneity Model for Water Exchange in the Brain: I. Theoretical Derivation. Journal of cerebral blood flow and metabolism : official journal of the International Society of Cerebral Blood Flow and Metabolism. 1998; 18(12):1365–1377.
21. Kuperman VYU, Karczmar GS, Blomley MJK, Lewis MZ, Lubich LM, Lipton MJ. Differentiating between T1 and T2* changes caused by gadopentetate dimeglumine in the kidney by using a double-echo dynamic MR imaging sequence. Journal of Magnetic Resonance Imaging. 1996; 6(5): 764–768. [PubMed: 8890014]
22. Quarles CC, Gore JC, Xu L, Yankeelov TE. Comparison of dual-echo DSC-MRI- and DCE-MRI-derived contrast agent kinetic parameters. Magn Reson Imaging. 2012; 30(7):944–953. [PubMed: 22617148]
23. Sourbron S, Heilmann M, Walczak C, Vautier J, Schad LR, Volk A. T2*-relaxivity contrast imaging: first results. Magn Reson Med. 2013; 69(5):1430–1437. [PubMed: 22733703]
24. Tofts PS. Modeling tracer kinetics in dynamic Gd-DTPA MR imaging. Journal of Magnetic Resonance Imaging. 1997; 7(1):91–101. [PubMed: 9039598]
25. Tofts PS, Brix G, Buckley DL, Evelhoch JL, Henderson E, Knopp MV, Larsson HBW, Lee TY, Mayr NA, Parker GJM, Port RE, Taylor J, Weisskoff RM. Estimating kinetic parameters from dynamic contrast-enhanced t1-weighted MRI of a diffusable tracer: Standardized quantities and symbols. Journal of Magnetic Resonance Imaging. 1999; 10(3):223–232. [PubMed: 10508281]
26. Tofts PS, Kermode AG. Measurement of the blood-brain barrier permeability and leakage space using dynamic MR imaging. 1. Fundamental concepts. Magn Reson Med. 1991; 17(2):357–367. [PubMed: 2062210]

27. Semmineh NB, Xu J, Boxerman JL, Delaney GW, Cleary PW, Gore JC, Quarles CC. An efficient computational approach to characterize DSC-MRI signals arising from three-dimensional heterogeneous tissue structures. PloS one. 2014; 9(1):e84764. [PubMed: 24416281]
28. Brix G, Bahner ML, Hoffmann U, Horvath A, Schreiber W. Regional Blood Flow, Capillary Permeability, and Compartmental Volumes: Measurement with Dynamic CT—Initial Experience. Radiology. 1999; 210(1):269–276. [PubMed: 9885619]
29. Schmiedeskamp H, Straka M, Newbould RD, Zaharchuk G, Andre JB, Olivot JM, Moseley ME, Albers GW, Bammer R. Combined spin- and gradient-echo perfusion-weighted imaging. Magn Reson Med. 2012; 68(1):30–40. [PubMed: 22114040]
30. Stokes AM, Skinner JT, Quarles CC. Assessment of a combined spin- and gradient-echo (SAGE) DSC-MRI method for preclinical neuroimaging. Magn Reson Imaging. 2014; 32(10):1181–1190. [PubMed: 25172987]
31. McGibney G, Smith MR, Nichols ST, Crawley A. Quantitative evaluation of several partial fourier reconstruction algorithms used in mri. Magn Reson Med. 1993; 30(1):51–59. [PubMed: 8371675]
32. Noll DC, Nishimura DG, Macovski A. Homodyne detection in magnetic resonance imaging. Medical Imaging, IEEE Transactions on. 1991; 10(2):154–163.
33. Landis CS, Li X, Telang FW, Coderre JA, Micca PL, Rooney WD, Latour LL, Vetek G, Palyka I, Springer CS. Determination of the MRI contrast agent concentration time course in vivo following bolus injection: Effect of equilibrium transcytolemmal water exchange. Magn Reson Med. 2000; 44(4):563–574. [PubMed: 11025512]
34. Rohrer M, Bauer H, Mintorovitch J, Requardt M, Weinmann HJ. Comparison of Magnetic Properties of MRI Contrast Media Solutions at Different Magnetic Field Strengths. Investigative Radiology. 2005; 40(11):715–724. [PubMed: 16230904]
35. Li X, Welch EB, Arlinghaus LR, Chakravarthy AB, Xu L, Farley J, Loveless ME, Mayer IA, Kelley MC, Meszoely IM, Means-Powell JA, Abramson VG, Grau AM, Gore JC, Yankeelov TE. A novel AIF tracking method and comparison of DCE-MRI parameters using individual and population-based AIFs in human breast cancer. Physics in medicine and biology. 2011; 56(17): 5753–5769. [PubMed: 21841212]
36. Hormuth DA 2nd, Skinner JT, Does MD, Yankeelov TE. A comparison of individual and population-derived vascular input functions for quantitative DCE-MRI in rats. Magn Reson Imaging. 2014; 32(4):397–401. [PubMed: 24556502]
37. Carroll TJ, Rowley HA, Haughton VM. Automatic Calculation of the Arterial Input Function for Cerebral Perfusion Imaging with MR Imaging1. Radiology. 2003; 227(2):593–600. [PubMed: 12663823]
38. Newton, AT.; Skinner, JT.; Quarles, CC. Automatic AIF Estimation in Multi-Echo DSC-MRI of Pediatric Patients - Avoiding the Noise Floor. Proceedings of the 21st Annual Meeting of ISMRM; Salt Lake City, UT, USA. 2013; p. 3064
39. Liu HL, Pu Y, Liu Y, Nickerson L, Andrews T, Fox PT, Gao JH. Cerebral blood flow measurement by dynamic contrast MRI using singular value decomposition with an adaptive threshold. Magn Reson Med. 1999; 42(1):167–172. [PubMed: 10398963]
40. Willats L, Calamante F. The 39 steps: evading error and deciphering the secrets for accurate dynamic susceptibility contrast MRI. Nmr Biomed. 2013; 26(8):913–931. [PubMed: 22782914]
41. Johnson G, Wetzel SG, Cha S, Babb J, Tofts PS. Measuring blood volume and vascular transfer constant from dynamic, T(2)*-weighted contrast-enhanced MRI. Magn Reson Med. 2004; 51(5): 961–968. [PubMed: 15122678]
42. Heye AK, Culling RD, Valdes Hernandez Mdel C, Thrippleton MJ, Wardlaw JM. Assessment of blood-brain barrier disruption using dynamic contrast-enhanced MRI. A systematic review. NeuroImage Clinical. 2014; 6:262–274. [PubMed: 25379439]
43. Sourbron SP, Buckley DL. Tracer kinetic modelling in MRI: estimating perfusion and capillary permeability. Physics in medicine and biology. 2012; 57(2):R1–33. [PubMed: 22173205]
44. Mangla R, Kolar B, Zhu T, Zhong J, Almast J, Ekholm S. Percentage signal recovery derived from MR dynamic susceptibility contrast imaging is useful to differentiate common enhancing malignant lesions of the brain. AJNR American journal of neuroradiology. 2011; 32(6):1004–1010. [PubMed: 21511863]

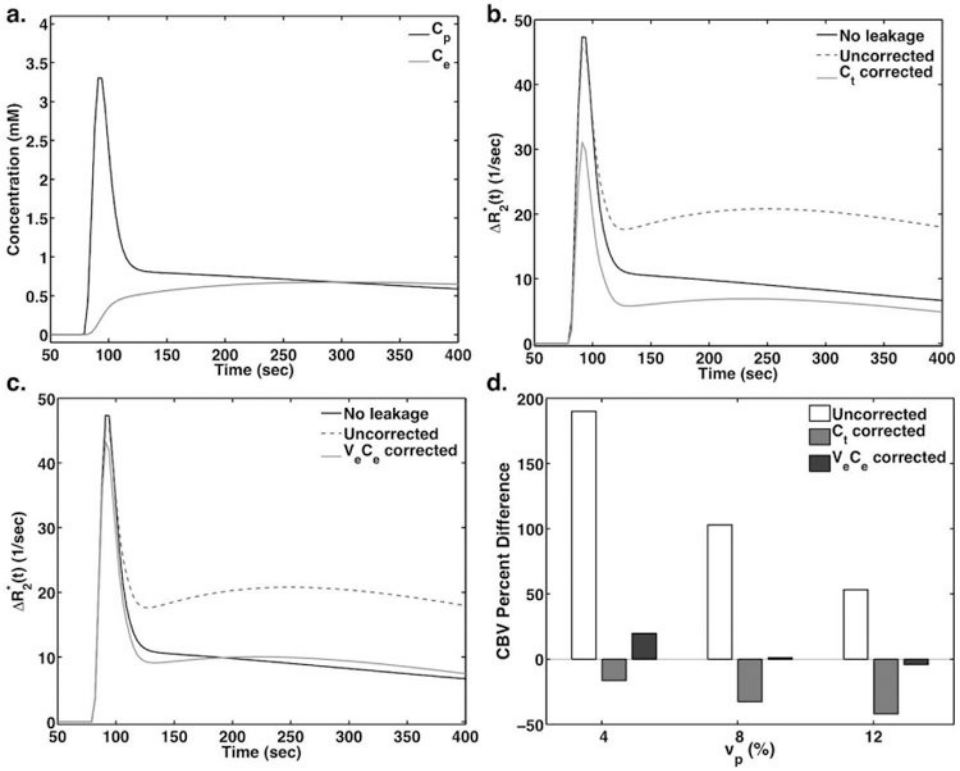

Figure 1.

(a) Simulated C_p and C_e curves for an 8% vascular volume fraction and 60% cell volume fraction using a two-compartment model and PFM. (b-c) Simulated ΔR_2* curves for no leakage, uncorrected, and corrected using $r_{2,t}^{*}C_t$ (b, Method 2) and $r_{2,e}^{*}v_eC_e$ (c, Method 3). (d) Bar plots showing the CBV percent difference between the true CBV and the uncorrected and corrected CBV.

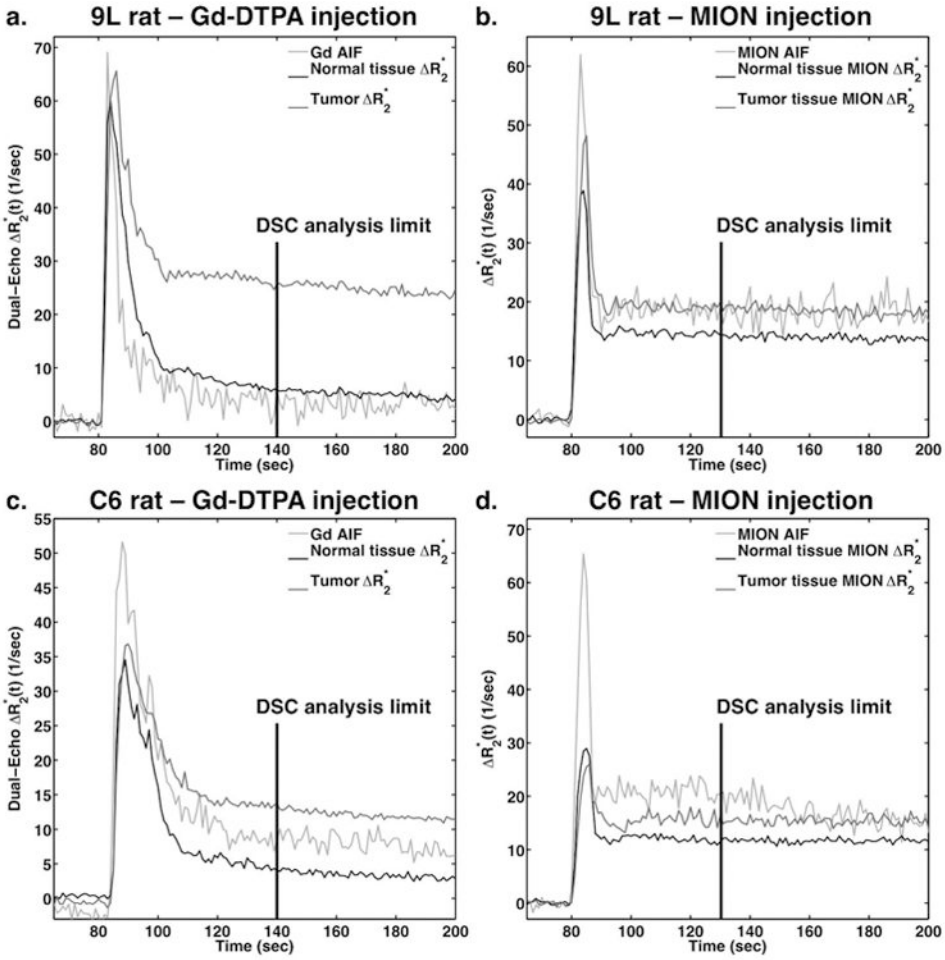

Figure 2.

Dynamic dual-echo ΔR_2* curves following bolus injection of Gd-DTPA (a,c) and MION (b,d) in 9L (a,b) and C6 (c,d) tumor ROIs. Normal tissue ROIs and AIFs are also shown for each tumor and contrast agent. DSC analysis was limited to 60 seconds post-injection for Gd-DTPA and 50 seconds post-injection for MION.

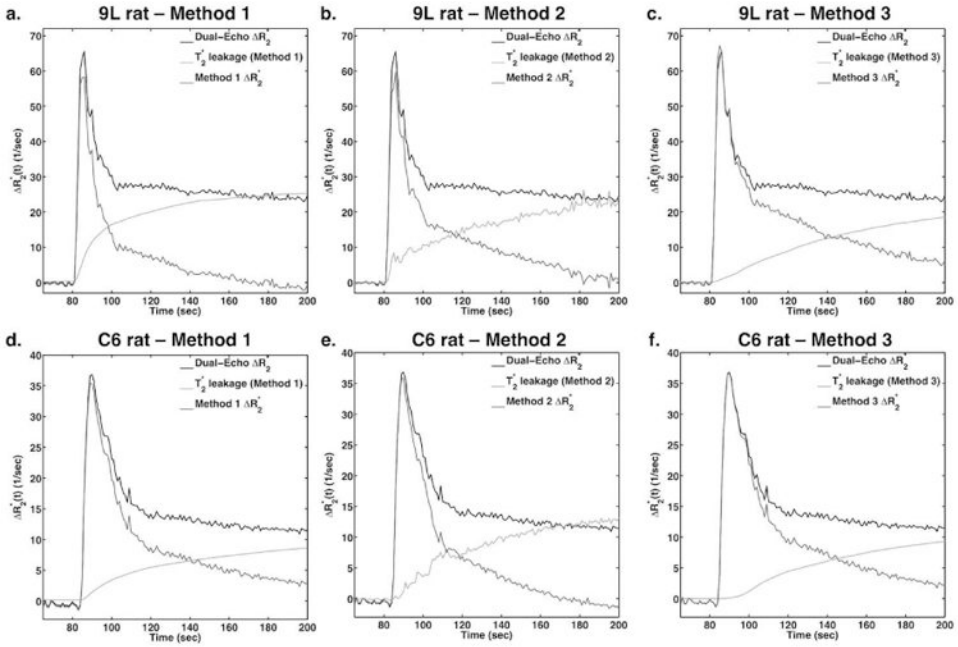

Figure 3.

Comparison of T_1- and T_2* leakage correction using Methods 1 (a,d), 2 (b,e), and 3 (c,f) in 9L (a-c) and C6 (d-f) tumor ROIs. For each panel, the T_1-corrected dual-echo ΔR_2* is shown, along with the T_2* leakage term derived from the leakage correction methods and the resulting corrected ΔR_2*.

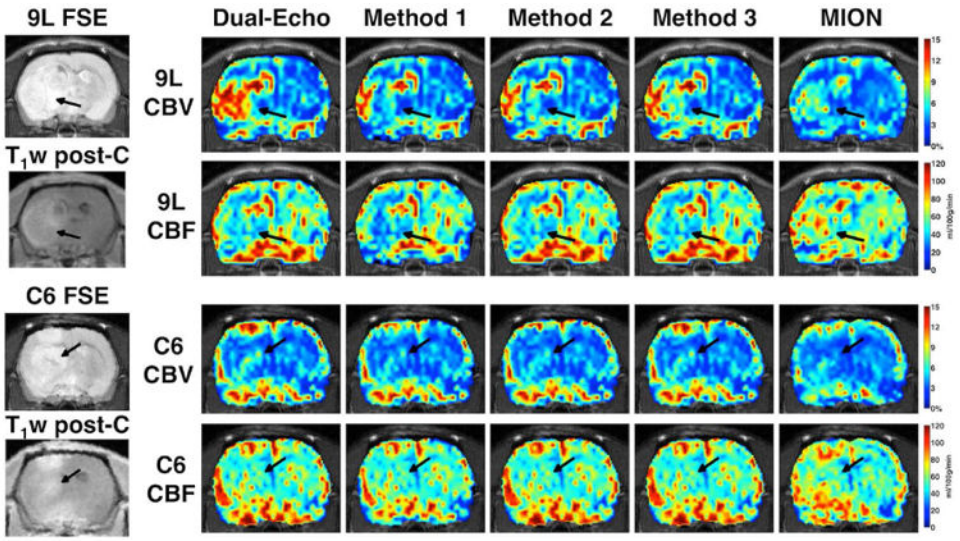

Figure 4.

T_1-corrected dual-echo, T_1- and T_2*-corrected (Methods 1, 2, and 3), and MION-based CBV and CBF in 9L (top) and C6 (bottom) tumor-bearing rats. Fast spin echo (FSE) and T_1-weighted post-contrast images show tumor location.

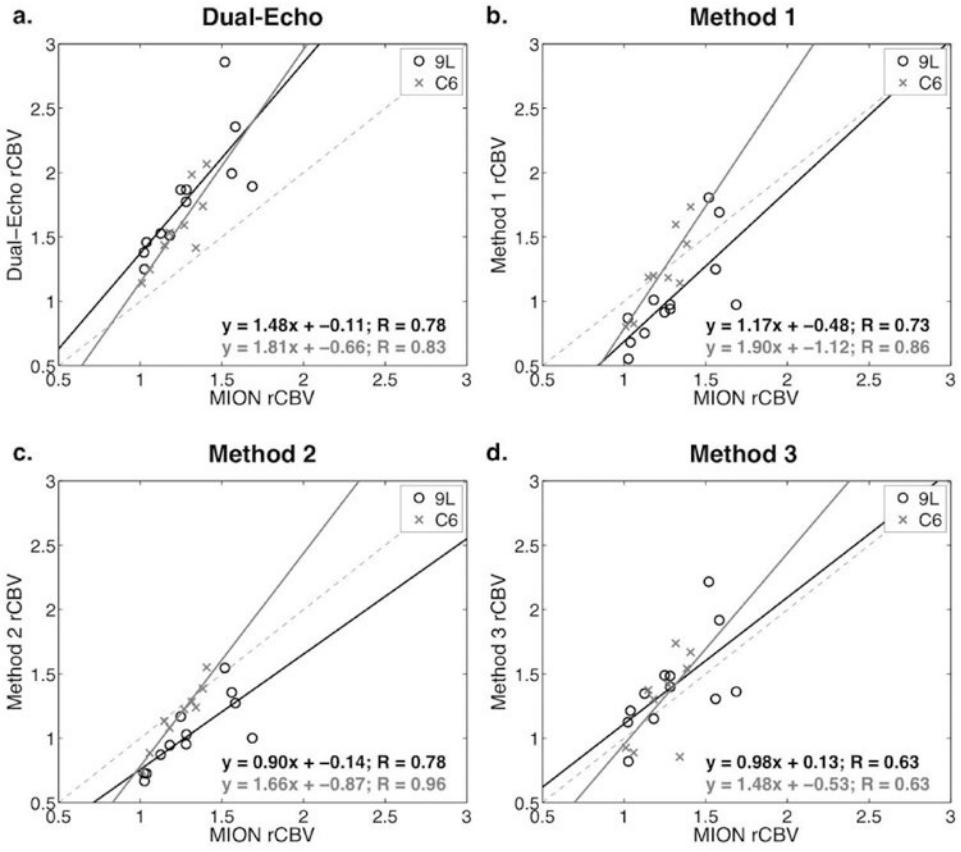

Figure 5.

Scatter plots showing rCBV from T_1-corrected dual-echo and Methods 1-3 (T_1- and T_2*-corrected) versus MION rCBV in 9L and C6 tumors. The 9L tumor values and linear regressions are shown in black, and the C6 tumor values and linear regressions are shown in gray.

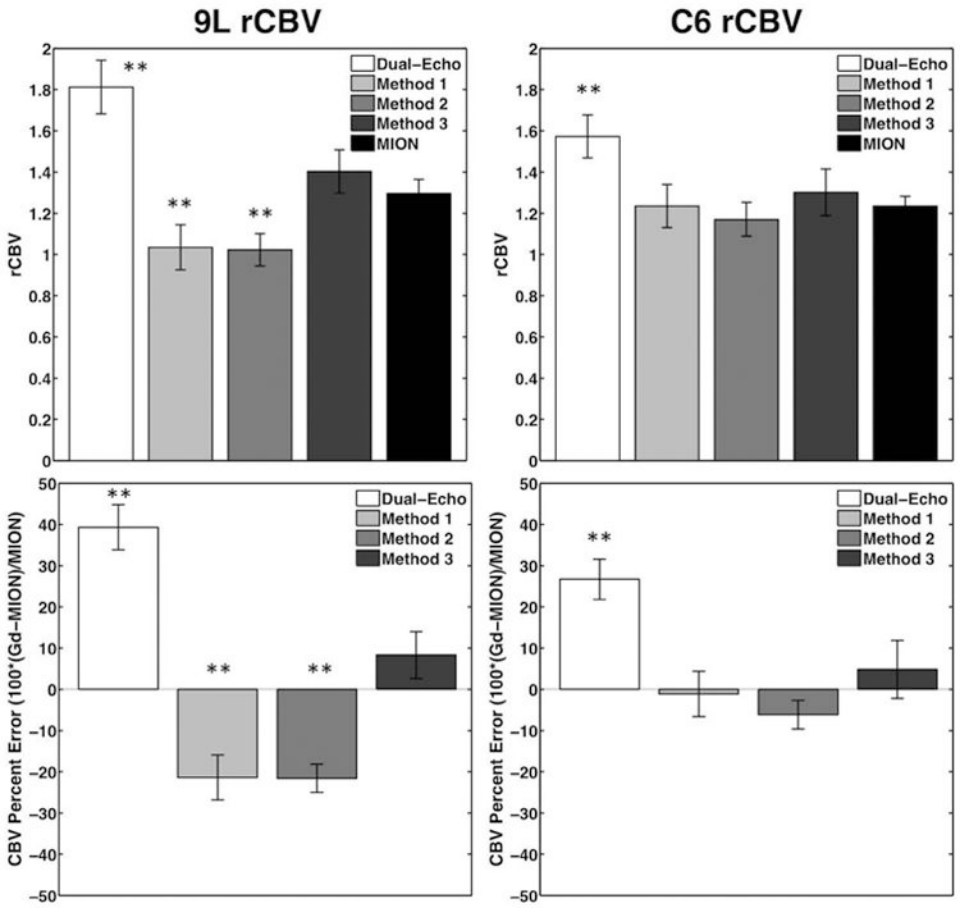

Figure 6.

Bar plots showing mean rCBV and CBV percent error in 9L (n=12) and C6 (n=9) tumors for T_1-corrected dual-echo, Methods 1, 2 and 3 (T_1- and T_2*-corrected), and MION reference. **p<0.01 and *p<0.05.

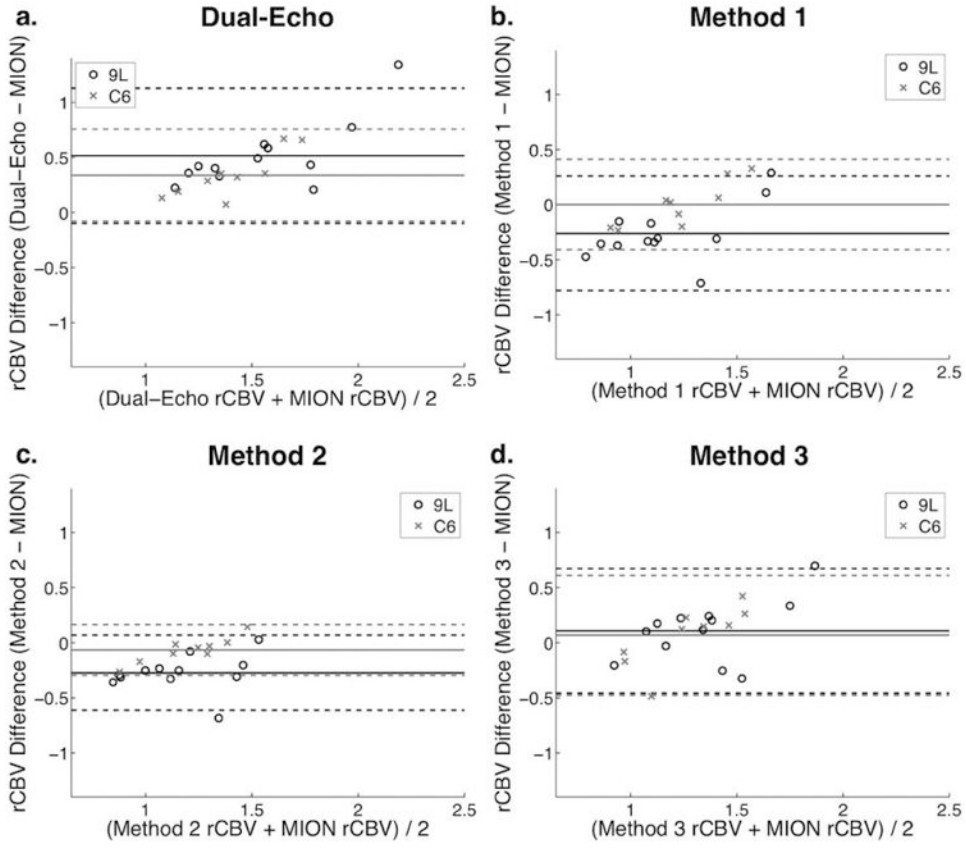

Figure 7.

Bland-Altman plots comparing dual-echo, Method 1, Method 2, and Method 3 rCBV with MION rCBV for 9L (open circles) and C6 tumors (x marks).

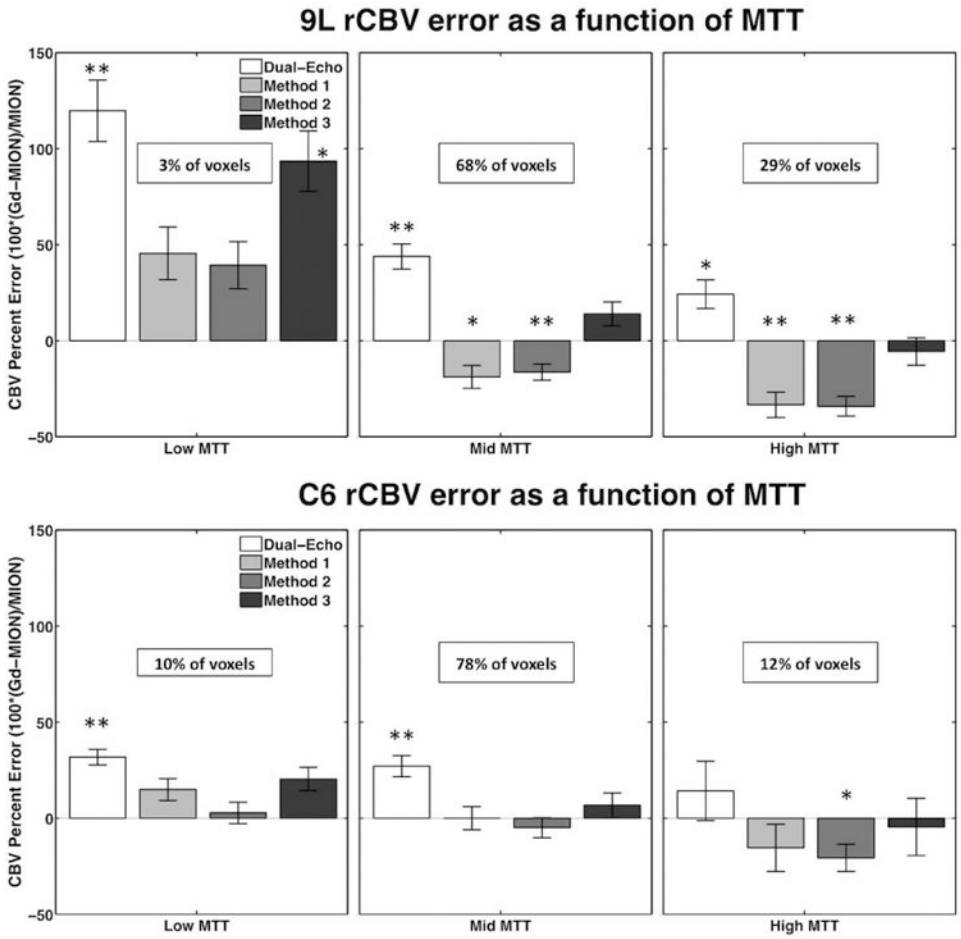

Figure 8.

Bar plots showing rCBV percent error (relative to MION rCBV) in 9L and C6 tumors as a function of MTT for dual-echo and Methods 1, 2, and 3. The percents of all voxels described by each bin (low, mid, and high MTT) are shown in each panel. **p<0.01 and *p<0.05.

Table 1

Relative CBV and CBF parameters in 9L and C6 tumors for dual-echo, correction methods 1-3, and MION. Slope, CCC, R, and p-values are obtained from each method versus MION.

		9L					C6				
	Method	**Mean (std)**	**slope[a]**	**CCC[a]**	**R[a]**	**P-value[a]**	**Mean (std)**	**slope[a]**	**CCC[a]**	**R[a]**	**P-value[a]**
rCBV	Dual-Echo	1.81 (0.45)	1.48	0.30	0.78	**0.003**	1.57 (0.31)	1.81	0.30	0.83	**0.006**
	Method 1	1.04 (0.38)	1.17	0.48	0.73	**0.007**	1.24 (0.32)	1.90	0.65	0.86	**0.003**
	Method 2	1.02 (0.27)	0.90	0.47	0.78	**0.003**	1.17 (0.25)	1.66	0.79	0.96	**<0.001**
	Method 3	1.40 (0.37)	0.98	0.54	0.63	**0.027**	1.30 (0.34)	1.48	0.43	0.63	0.07
	MION	1.30 (0.24)	--	--	--	--	1.23 (0.14)	--	--	--	--
rCBF	Dual-Echo	0.88 (0.20)	0.51	0.40	0.54	0.07	1.13 (0.18)	0.37	0.34	0.43	0.25
	Method 1	0.83 (0.20)	0.49	0.32	0.51	0.09	1.08 (0.19)	0.44	0.33	0.47	0.20
	Method 2	0.81 (0.18)	0.49	0.31	0.57	0.05	1.07 (0.17)	0.36	0.27	0.44	0.24
	Method 3	0.87 (0.19)	0.48	0.37	0.52	0.08	1.10 (0.20)	0.31	0.23	0.32	0.40
	MION	1.04 (0.21)	--	--	--	--	1.26 (0.20)	--	--	--	--

std: standard deviation; CCC: concordance correlation coefficient; R: Pearson's correlation coefficient;

[a]between each method and MION